ORIGINAL PAPER

Volker Gravemeier

Variational multiscale large eddy simulation of turbulent flow in a diffuser

Abstract In the present study, variational multiscale large eddy simulation (LES) is applied to turbulent flow in a diffuser, which represents a challenging test case due to the appearance of flow separation and subsequent reattachment. Two different scale-separating operators based on multigrid operators are used for separating large and small resolved scales. Dynamic as well as constant-coefficient-based subgrid-scale modeling are employed in the variational multiscale LES. The results show that the variational multiscale LES with a simple constant-coefficient Smagorinsky model using a projective scale-separating operator yields a very good prediction of most of the crucial flow features. Furthermore, it turns out to be by far the most computationally efficient approach, resulting in a computing time reduction of about 18% compared to the traditional LES with a dynamic Smagorinsky model. The variational multiscale LES with a dynamic Smagorinsky model does not prove to be a superior approach.

Keywords Turbulence · Large eddy simulation · Variational multiscale method · Scale separation · Diffuser

1 Introduction

Large eddy simulation (LES) represents an approach for the numerical simulation of turbulent flows aiming at a complete resolution of only the large-scale structure of the flow. The effect of the unresolved scales on the resolved scales is modeled. Thus, a basic ingredient of the approach consists of the

V. Gravemeier
Center for Turbulence Research,
Stanford University, Stanford, CA 94305, USA

V. Gravemeier (✉)
Chair for Computational Mechanics,
Technical University of Munich, Boltzmannstr. 15,
85747 Garching, Germany
E-mail: vgravem@lnm.mw.tum.de
Tel.: +49-89-28915245
Fax: +49-89-28915301

separation of resolved and unresolved scales. The general concept of the variational multiscale method involves separating the problem scales into a predefined number of scale groups. This theoretical framework was also applied to the incompressible Navier–Stokes equations in [18], in order to facilitate LES of turbulent incompressible flows. The concept in [18] assumes a separation of two scale groups. In [4] and [12], a three-scale separation accounting for large resolved scales, small resolved scales, and unresolved scales was proposed, which explicitly identified the unresolved scales of the problem as an additional independent scale group. A comprehensive review of the variational multiscale method for LES has recently been provided in [11].

Two important aspects characterize the variational multiscale LES. Firstly, a variational projection separates scale ranges within the variational multiscale LES rather than a spatial filter in the traditional LES. Secondly, the (direct) influence of the subgrid-scale model, which is introduced to represent the effect of the unresolved scales on the resolved scales, is confined to the small resolved scales. Thus, the larger scales are solved as a direct numerical simulation (DNS) (i.e., without any (direct) influence of the modeling term). Of course, the large resolved scales are still indirectly influenced by the subgrid-scale model due to the inherent coupling of all scales. Various test cases have been studied in the meantime, to investigate the performance of the variational multiscale method in practical applications, and good results have been achieved to a large extent. However, most of these studies have been within simpler configurations. In the following, a brief overview of the flow problems addressed so far will be given along with the respectively applied numerical methods and the respective approach for separating the scale groups.

The simplest turbulent flow problem and, thus, a well-suited initial test case is homogeneous isotropic turbulence. Hughes et al. [19] presented simulations of this flow, using a spectral method. Applications of the variational multiscale LES in the spectral space can be executed in a straightforward manner, with the sharp (or spectral) cutoff filter as the "tool" for scale separation. The sharp cutoff filter provides

a projective scale separation in the spectral space. The same flow situation was investigated in [23], applying a continuous Galerkin finite element method with hierarchical shape function bases. In that study, shape functions up to a certain polynomial order represented the large scales, and the remaining shape functions up to the level of resolution were supposed to capture the smaller scales. This may similarly be done using a discontinuous Galerkin finite element method, as proposed in [5]. In the classical notation of finite element methods, such methods may be denoted as "*p*-type" scale separations (i.e., based on the polynomial order of the approximation). In two recent studies, the influence of the resolution level [21] as well as the applied numerical method [35] on the energy transfer in the context of homogeneous isotropic turbulence were investigated.

Turbulent channel flow is the most famous representative of the test cases exhibiting one inhomogeneous flow direction. This test case was addressed in [20] and [34], applying a spectral method in the homogeneous planes of the channel and modified Legendre polynomials in the inhomogeneous wall-normal direction. As in their work on homogeneous isotropic turbulence, the sharp cutoff filter in Fourier space enabled the separation of scales. With a similar approach in the homogeneous planes and fourth-order spectral-like compact finite differences in the inhomogeneous direction, the channel flow problem was simulated in [24]. In their regularized version of the variational multiscale LES, those authors used the discrete top-hat filter for the extraction of those small resolved scales which the subgrid-scale model is applied to. Discrete smooth filters do not provide a projective scale separation. Therefore, this regularized version only fulfills the second of the two aforementioned prerequisites for the variational multiscale LES (i.e., the restriction of the direct influence of the subgrid-scale model to the small resolved scales). Interestingly, a combination of the sharp cutoff filter in the homogeneous planes and projective sampling procedures in the inhomogeneous wall-normal direction were employed for the dynamic modeling procedure in [24]. Another recent study only fulfilling the second prerequisite for the variational multiscale LES was [39], which also applied a discrete smooth filter for scale separation. The author of that study used a second-order energy-conserving finite difference method for the channel flow simulations.

Further test cases beside these two flow situations have been studied in the meantime. The turbulent flow in a lid-driven cavity was investigated in [12], using a three-level finite element method. Two important features are linked with this approach. On the one hand, the large- and the small-scale equation, which are eventually achieved as a result of applying the variational multiscale method, are solved as a coupled system of two equations, updating their mutual dependence in an iterative procedure. On the other hand, a localized approach is chosen on the small-scale level. This choice makes this approach very efficient from the computational point of view, but substantially limits the potential amount of small scales captured due to the neglect of non-local interdependencies within the small scales. The flow problem of a plane mixing layer was also simulated via the three-level finite element method in [12]. A three-dimensional mixing layer and turbulent flow past a square cylinder was investigated in [25], using another *p*-type scale separation in the context of a continuous Galerkin finite element method. A combined finite volume/element method was applied in [28] for the numerical simulation of turbulent flow past a square cylinder and in [8] for the simulation of turbulent flow past a prolate spheroid and a forward swept scaled wing. The scale separation based on volume-agglomeration used in those studies is very similar to the strategy which is used in the present study. Recently, a new residual-based variant of the variational multiscale LES was developed and tested on the problem of bypass transition of a boundary layer in [3]. This new residual-based variant, however, does not fulfill the second prerequisite of the variational multiscale method. Therefore, a separation of two scale groups within the range of resolved scales is no longer necessary.

The predecessor of the present work is the study in [10]. In that study, a class of scale-separating operators based on multigrid operators was proposed and analyzed. In contrast to [24], the scale-separating operators were consistently used for both the extraction of the small scales, which the subgrid-scale model is applied to, and any scale separation necessary for a dynamic modeling procedure. All scale-separating operators were implemented in the CDP-α code, the flagship LES code of the Center for Turbulence Research, see [15] for some basic features of this code. Underlying this code is a second-order energy-conserving finite volume method particularly suited for applications on unstructured colocated grids. A comparison of two representatives of the proposed class of multigrid scale-separating operators with discrete smooth filters revealed its superiority, both in terms of quality of results and required computational effort. This superiority was particularly significant for one of these two scale-separating operators. This particular operator was shown to provide a projective scale separation in [10]. It is essentially the same operator used in [8] and [28], although those authors pursued the converse path in terms of grid generation. They started from an initial discretization representing the complete resolution level and identified the large-scale level through a volume-agglomeration procedure afterwards. In contrast, it is started with an initial discretization representing the large-scale resolution level in [10]. Afterwards, isotropic hierarchical subdivision yielded the discretization representing the complete resolution level. Nevertheless, both approaches may be labeled as "*h*-type" scale separations (i.e., based on the discretization, which is characterized by the length scale *h*).

In the present study, the scale-separating operators based on multigrid operators, which proved their success in terms of quality of results and computational efficiency for turbulent channel flow in [10], are applied to turbulent flow in a planar asymmetric diffuser. The Reynolds number of the investigated flow is about 10,000, based on the half-width of the inlet channel and the streamwise bulk mean velocity. Turbulent flow in such a diffuser is a representative of the group of flow problems exhibiting more than one direction
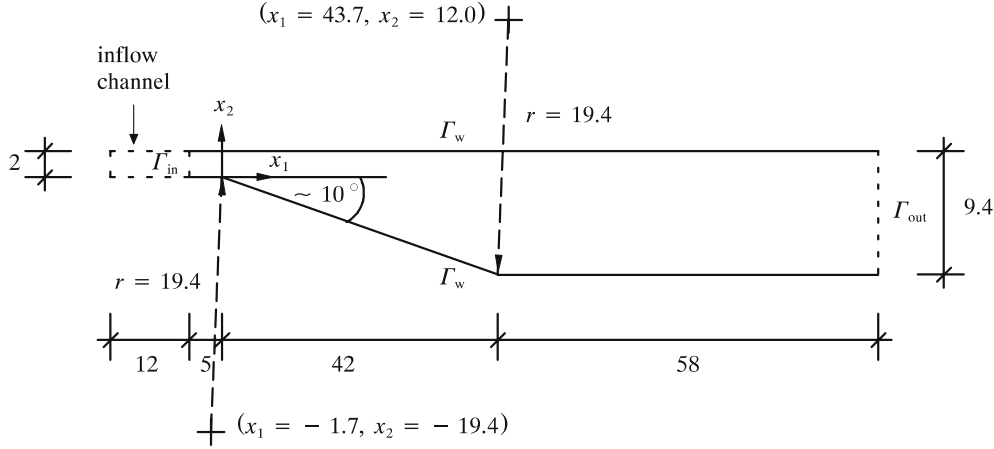
Fig. 1 Diffuser geometry in x_1–x_2-plane

of inhomogeneity. Not only for this reason, it is a more challenging flow problem. Several features of this flow indicate its higher complexity. Three of them should be explicitly named in the following.

- A large unsteady separation bubble due to an adverse pressure gradient emerges about halfway down the lower deflected wall. The flow reattaches within the outlet channel.
- The streamwise pressure gradient changes suddenly from slightly favorable to strongly adverse at the diffuser throat and gradually decreases to weakly adverse afterwards.
- A slowly growing internal layer emerges at the upper flat wall in the relaxation zone downstream of the sharp variation in the streamwise pressure gradient according to the recent numerical study in [40].

Experimental studies of turbulent flow in a planar asymmetric diffuser were presented, for instance, in [2,36], and recently in [13]. A DNS of the flow at this Reynolds number in the present diffuser configuration is still prohibitively expensive. Large eddy simulations were conducted in [26] and recently in [40]. Numerical investigations of this case using simulations based on the Reynolds-averaged Navier–Stokes equations were described in [1,7,13], and [22]. The diffuser problem was also a test case at a workshop [17] in 1999. Among other things, the fact that the prediction of the separation and the extent of the recirculation region is particularly challenging for computational models had led to choosing this example as the object of consideration in this workshop. Those observations also provide the motivation for investigating this flow problem as a challenging test case for the variational multiscale LES in the present study.

The remainder of this study is organized as follows. In Sect. 2, the problem of the incompressible Navier–Stokes equations is stated for the diffuser, with appropriate initial and boundary conditions. Afterwards, the basic variational formulation for a finite volume method is given. The separation of scales using multigrid operators and the multiscale formulation based on this scale separation are described in Sect. 3. Subgrid-scale modeling for the variational multiscale LES is briefly addressed in Sect. 4. Section 5 contains

the numerical simulation results from the application of the variational multiscale LES to the turbulent flow in a planar asymmetric diffuser. Among other things, they are compared to experimental results as well as results from the recent LES study of this flow problem in [40]. Finally, conclusions are drawn in Sect. 6.

2 Problem statement and variational finite volume formulation

The set of incompressible Navier–Stokes equations is given as

$$\frac{\partial \mathbf{u}}{\partial t} + \nabla \cdot (\mathbf{u} \otimes \mathbf{u}) + \nabla p - \nu \Delta \mathbf{u} = \mathbf{0} \quad \text{in } \Omega \times (0, T), \quad (1)$$

$$\nabla \cdot \mathbf{u} = 0 \qquad \qquad \text{in } \Omega \times (0, T), \quad (2)$$

where $\mathbf{u}$ denotes the velocity vector, p the kinematic pressure (i.e., pressure divided by density), ν the kinematic viscosity, Ω the spatial domain of the diffuser, and T the simulation time. The diffuser geometry in the $x_1 - x_2$-plane is depicted in Fig. 1.

A zero velocity field as

$$\mathbf{u} = 0 \quad \text{in } \Omega \times \{0\} \tag{3}$$

is assumed to be the initial condition for the velocity, which obviously fulfills the condition of being divergence-free. A Dirichlet boundary condition reading

$$\mathbf{u} = \mathbf{g} \quad \text{on } \Gamma_g \times (0, T), \tag{4}$$

is prescribed on the subset Γ_g of the domain boundary Γ. The Dirichlet boundary Γ_g covers the inflow boundary Γ_{in} as well as the upper and lower walls Γ_{w} of the diffuser, see Fig. 1. At the walls Γ_{w}, no-slip boundary conditions (i.e., $\mathbf{g} = 0$) are assumed throughout the simulation time T. At the inflow boundary Γ_{in}, a time-dependent inflow velocity vector $\mathbf{g} = \mathbf{u}^{\text{in}}(t)$ is prescribed. At the outflow boundary Γ_{out}, a convective boundary condition is prescribed subject to

$$\frac{\partial \mathbf{u}}{\partial t} + u^{\text{out}} \frac{\partial \mathbf{u}}{\partial x_1} = 0 \quad \text{on } \Gamma_{\text{out}} \times (0, T), \tag{5}$$

where u^{out} is calculated such that overall conservation is maintained (i.e., the mass flux through the outflow boundary equals the mass flux through the inflow boundary). Finally, periodic boundary conditions are assumed on the boundaries Γ_{per} in x_3-direction (i.e., this periodicity is assumed orthogonal to the depiction in Fig. 1).

A weighted residual formulation of the Navier–Stokes equations is given as follows: find $\{\mathbf{u}, p\} \in \mathscr{S}_{\mathbf{u}p}$, such that

$$B_{\text{NS}}(v, q; \mathbf{u}, p) = (v, f)_\Omega \quad \forall\{v, q\} \in \mathscr{V}_{\boldsymbol{u}p}, \tag{6}$$

where v and q denote the weighting functions. $\mathscr{S}_{\mathbf{u}p}$ and $\mathscr{V}_{\mathbf{u}p}$ represent the combined formulation of the solution and weighting function spaces for velocity and pressure: $\mathscr{S}_{\mathbf{u}p} := \mathscr{S}_{\mathbf{u}} \times \mathscr{S}_p$ and $\mathscr{V}_{\boldsymbol{u}p} := \mathscr{V}_{\mathbf{u}} \times \mathscr{V}_p$, respectively. The L_2-inner product in the domain Ω on the right hand side of (6) is defined as usual:

$$(v, f)_\Omega = \int_\Omega v f \, \mathrm{d}\Omega. \tag{7}$$

Using the notation in (7), the form $B_{\text{NS}}(v, q; \mathbf{u}, p,)$ on the left-hand side of (6), which is linear on the first slot (i.e., v, q) and non-linear on the second slot (i.e., $\mathbf{u}, p$), is defined as

$$B_{\text{NS}}(v, q; \mathbf{u}, p) = \left(v, \frac{\partial \mathbf{u}}{\partial t}\right)_\Omega + (v, \nabla \cdot (\mathbf{u} \otimes \mathbf{u}))_\Omega$$
$$+ (v, \nabla p)_\Omega - (v, \nu \Delta \mathbf{u})_\Omega + (q, \nabla \cdot \mathbf{u})_\Omega. \tag{8}$$

The domain Ω is now discretized into n control volumes $\Omega_i (i = 1, \ldots, n)$, with control volume boundaries Γ_i. The weighting functions are chosen to be

$$v^h = \sum_i v_i^h, \quad q^h = \sum_i q_i^h, \tag{9}$$

where

$$v_i^h = \mathbf{1}, \quad q_i^h = 1 \text{ in } \Omega_i \tag{10}$$

and zero elsewhere. In (10), $\mathbf{1}$ explicitly means that each component of v_i^h is of unit value. The characteristic control volume length of the discretization is h. With these definitions at hand, the weighted residual equation (6) may be reformulated as a variational finite volume equation for each v_i^h and q_i^h: find $\{\mathbf{u}^h, p^h\} \in \mathscr{S}_{\mathbf{u}p}^h$, such that

$$B_{\text{NS}}^{\text{FV}}\left(v_i^h, q_i^h; \mathbf{u}^h, p^h\right) = \left(v_i^h, f\right)_\Omega. \tag{11}$$

Defining

$$(v, f)_{\Gamma_i} = \int_{\Gamma_i} v f \, \mathrm{d}\Gamma \tag{12}$$

analogous to (7), where Γ_i denotes the boundary of the support of v_i^h and q_i^h, respectively, the semi-linear form $B_{\text{NS}}^{\text{FV}}\left(v^h, q_i^h; \mathbf{u}^h, p^h\right)$ on the left-hand side of (11) is obtained from (8) after applying Gauss' theorem to the convective term, the pressure term, the viscous term, and the continuity term as

$$B_{\text{NS}}^{\text{FV}}\left(v_i^h, q_i^h; \mathbf{u}^h, p^h\right) = \left(v_i^h, \frac{\partial \mathbf{u}^h}{\partial t}\right)_\Omega + \left(v_i^h, \left(\mathbf{u}^h \otimes \mathbf{u}^h\right) \cdot \mathbf{n}\right)_{\Gamma_i}$$
$$+ \left(v_i^h, p^h \mathbf{n}\right)_{\Gamma_i} - \left(v_i^h, v \left(\nabla \mathbf{u}^h\right) \cdot \mathbf{n}\right)_{\Gamma_i}$$
$$+ \left(q_i^h, \mathbf{u}^h \cdot \mathbf{n}\right)_{\Gamma_i}. \tag{13}$$

In (13), $\mathbf{n}$ indicates the respective outward normal vector of unit length to Γ_i.

The characteristic length scale h chosen in LESs is usually considerably larger than the smallest length scale of the problem under investigation (i.e., by far not all scales of the problem can be resolved). Therefore, the subgrid viscosity approach, a usual way of taking into account the (dissipative) effect of unresolved scales in the traditional LES, is applied. According to this, a subgrid viscosity term is added to (11), resulting in

$$B_{\text{NS}}^{\text{FV}}\left(v_i^h, q_i^h; \mathbf{u}^h, p^h\right) - \left(v_i^h, v_{\text{T}} \left(\nabla \mathbf{u}^h\right) \cdot \mathbf{n}\right)_{\Gamma_i} = \left(v_i^h, f\right)_\Omega, \tag{14}$$

where v_{T} denotes the subgrid viscosity. Note that the subgrid viscosity term is added to *all* resolved scales of the problem in (14). Note also that the reason for introducing a model term in this context is mathematically different from the usual necessity of introducing a model term due to the appearance of a subfilter-scale (or subgrid-scale) stress tensor in the strong formulation of the Navier–Stokes equations in a traditional LES. Nevertheless, the physical necessity of accounting for the missing effect of unresolved scales on the resolved scales is the same in both the traditional and the variational multiscale LES.

3 Separation of scales and multiscale formulation

The resolved velocity vector $\mathbf{u}^h$ is separated into a large-scale part and a small-scale part subject to

$$\mathbf{u}^h = \left(\bar{\mathbf{u}} + \mathbf{u}'\right)^h. \tag{15}$$

With respect to this complete resolution level, a large-scale resolution level is identified a priori. This level is characterized by the characteristic control volume length $\bar{h}$, where $\bar{h} > h$, and, accordingly, yields a large-scale velocity $\bar{\mathbf{u}}^{\bar{h}}$. The small-scale velocity is consistently defined on the complete resolution level, characterized by the length h, as

$$\mathbf{u}'^h = \mathbf{u}^h - \bar{\mathbf{u}}^h, \tag{16}$$

where $\bar{\mathbf{u}}^h$ denotes the large-scale value transferred to this level. The scale separation used in the present study relies on multigrid operators. At the outset of the numerical simulation, two grids are created: a coarser grid, which is called the "parent" grid, and a finer grid, which is called the "child" grid. The child grid is obtained by an isotropic hierarchical subdivision of the parent grid. In the simulations of the present study, a subdivision by a factor of two in each spatial direction is exclusively applied. For more details concerning the implementation, it is referred to [10].

The general class of scale-separating operators based on multigrid operators is formulated as

$$\bar{\mathbf{u}}^h = S^{\mathrm{m}}\left[\mathbf{u}^h\right] = P \circ R\left[\mathbf{u}^h\right] = P\left[\bar{\mathbf{u}}^{\bar{h}}\right], \tag{17}$$

where the multigrid scale-separating operator S^{m} consists of the sequential application of a restriction operator R and a prolongation operator P. Applying the restriction operator on $\mathbf{u}^h$ yields a large-scale velocity $\bar{\mathbf{u}}^{\bar{h}}$ defined at the degrees of freedom of the parent grid, which is then prolongated, in order to obtain a large-scale velocity $\bar{\mathbf{u}}^h$ defined at the degrees of freedom of the child grid. Various restriction as well as prolongation operators may be used in (17). Two special combinations of restriction and prolongation operators were analyzed and compared to discrete smooth filters, which are widely used in traditional LES, in [10]. It was shown that these two multigrid scale-separating operators represent computationally efficient operators for separating the resolved scales of the problem in comparison to discrete smooth filters. Both multigrid scale-separating operators rely on the same restriction operator, but apply different prolongation operators afterwards.

The restriction operator is defined to be a volume-weighted average over all the child control volumes within one parent control volume subject to

$$\bar{\mathbf{u}}_j^{\bar{h}} = \frac{\sum_{i=1}^{n_{\mathrm{cop}}} |\Omega_i| \mathbf{u}_i^h}{\sum_{i=1}^{n_{\mathrm{cop}}} |\Omega_i|}, \tag{18}$$

where $\bar{\mathbf{u}}_j^{\bar{h}}$ denotes the large-scale velocity at the center of the parent control volume $\bar{\Omega}_j$ and n_{cop} the number of child control volumes in $\bar{\Omega}_j$. The first prolongation operator P^{p} yields a constant prolongation, which is given as

$$\bar{\mathbf{u}}_i^h = P^{\mathrm{p}}\left[\bar{\mathbf{u}}_j^{\bar{h}}\right]_i = \bar{\mathbf{u}}_j^{\bar{h}} \quad \forall\, \Omega_i \subset \bar{\Omega}_j \tag{19}$$

and zero elsewhere. It was shown in [10] that the scale-separating operator defined as

$$S^{\mathrm{pm}} := P^{\mathrm{p}} \circ R \tag{20}$$

has the property of a projector, which is indicated by the additional superscript "p". The projector (20) is exactly the operator also used in [8,28], although it was not derived from the general formulation (17) and, thus, not split up into a restriction and prolongation operator in those studies.

The second prolongation operator considered in the present study yields a linear prolongation subject to

$$\bar{\mathbf{u}}_i^{\bar{h}} = P^{\mathrm{s}}\left[\bar{\mathbf{u}}_j^{\bar{h}}\right]_i = \bar{\mathbf{u}}_j^{\bar{h}} + \left(\nabla^{\bar{h}} \bar{\mathbf{u}}_j^{\bar{h}}\right) \cdot \left(\mathbf{r}_i - \bar{\mathbf{r}}_j\right) \quad \forall\, \Omega_i \subset \bar{\Omega}_j \tag{21}$$

and zero elsewhere. The vectors $\mathbf{r}_i$ and $\bar{\mathbf{r}}_j$ denote geometrical vectors pointing to the centers of the child control volume Ω_i and the parent control volume $\bar{\Omega}_j$, respectively. $\nabla^{\bar{h}}$ describes the discrete gradient operator on the parent grid. Due to this, values from neighboring parent control volumes and, consequently, child control volumes contained in these neighboring parent control volumes influence the final large-scale value in the child control volume Ω_i. The prolongation P^{s} does not provide us with a projective scale-separating operation. It rather produces a smoothing prolongation, which is, at least, smoother than the prolongation produced by P^{p}. Thus, it is

indicated by the additional superscript "s", and the complete scale-separating operator is defined as

$$S^{\mathrm{sm}} := P^{\mathrm{s}} \circ R. \tag{22}$$

For the actual scale separation within a variational finite volume formulation, a large-scale velocity weighting function as

$$\bar{v}^{\bar{h}} = \sum_i \bar{v}_i^{\bar{h}}, \tag{23}$$

where

$$\bar{v}_i^{\bar{h}} = 1 \quad \text{in } \bar{\Omega}_i \tag{24}$$

and zero elsewhere, is introduced analogous to the large-scale velocity solution function. $\bar{\Omega}_i$ denotes the ith control volume of the discretization with the characteristic control volume length $\bar{h}$. The separation of the weighting functions enables a decomposition of the variational equation (11) into a large- and a small-scale equation. The coupled system of large- and small-scale equation, resulting from an initial three-scale separation, may be found, for instance, in [11]. For the particular scale separation used in the present work, these two equations may eventually be reunified to *one* final equation, see, e.g., [11]. In this final equation, the scale separation based on S^{m} has to be applied only to the subgrid viscosity term. Based on the variational finite volume formulation (14), the following problem statement for each v_i^h, q_i^h, and $\bar{v}_i^{\bar{h}}$, where the child grid control volume Ω_i is contained in the parent grid control volume $\bar{\Omega}_i$ is obtained: find $\{\mathbf{u}^h, p^h\} \in \mathscr{S}_{\mathbf{u}_p}^h$, such that

$$
\begin{aligned}
&B_{\mathrm{NS}}^{\mathrm{FV}}\left(v_i^h, q_i^h; \mathbf{u}^h, p^h\right) - \left(v_i'^h, v_{\mathrm{T}}'\left(\nabla \mathbf{u}'^h\right) \cdot \mathbf{n}\right)_{\Gamma_i'} \\
&= B_{\mathrm{NS}}^{\mathrm{FV}}\left(v_i^h, q_i^h; \mathbf{u}^h, p^h\right) - \left(v_i^h, v_{\mathrm{T}}'\left(\nabla\left(\mathbf{u}^h - \bar{\mathbf{u}}^h\right)\right) \cdot \mathbf{n}\right)_{\Gamma_i} \\
&\quad + \left(\bar{v}_i^{\bar{h}}, v_{\mathrm{T}}'\left(\nabla\left(\mathbf{u}^h - \bar{\mathbf{u}}^h\right)\right) \cdot \mathbf{n}\right)_{\bar{\Gamma}_i} \\
&= B_{\mathrm{NS}}^{\mathrm{FV}}\left(v_i^h, q_i^h; \mathbf{u}^h, p^h\right) - \left(v_i^h, v_{\mathrm{T}}'\left(\left(\nabla \mathbf{u}^h\right) \cdot \mathbf{n} - \left(\nabla \bar{\mathbf{u}}^h\right) \cdot \mathbf{n}\right)\right)_{\Gamma_i} \\
&\quad + \left(\bar{v}_i^{\bar{h}}, v_{\mathrm{T}}'\left(\left(\nabla \mathbf{u}^h\right) \cdot \mathbf{n} - \left(\nabla \bar{\mathbf{u}}^h\right) \cdot \mathbf{n}\right)\right)_{\bar{\Gamma}_i} \\
&= \left(v_i^h, f\right)_{\Omega},
\end{aligned}
\tag{25}
$$

where v'^h denotes the small-scale part of the velocity weighting function and v_{T}' the subgrid viscosity depending on the small resolved scales, to be defined below. The boundary Γ_i is split up into a large-scale boundary $\bar{\Gamma}_i$ and, accordingly, a small-scale boundary subject to

$$\Gamma_i' = \Gamma_i - \bar{\Gamma}_i. \tag{26}$$

In Fig. 2, the definition of large- and small-scale boundaries in the FVM is illustrated for the two-dimensional case. The large-scale weighting function $\bar{v}^{\bar{h}}$ is exclusively defined on the large-scale boundaries belonging to the parent control volume, as shown in Fig. 2a. The small-scale weighting function v'^h has non-zero values only on the inner boundaries of the child control volumes, see Fig. 2b.
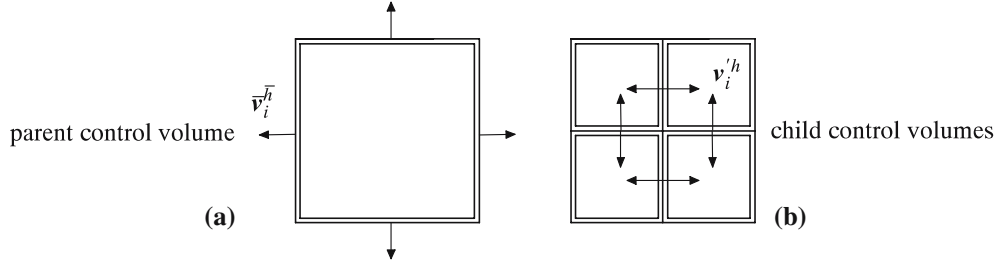
Fig. 2 Geometrical locations of weighting functions in the finite volume method (two-dimensional case): (**a**) large-scale weighting function; (**b**) small-scale weighting function

For one of the scale-separating operators (i.e., S^{pm}), a further simplification of (25) is accomplishable. A crucial difference between S^{pm} and S^{sm} consists of the fact that there is no large-scale (subgrid) viscous flux for S^{pm} across the small-scale boundary subject to (26). As a result, (25) may be specified for S^{pm} as

$$B_{\mathrm{NS}}^{\mathrm{FV}}\left(v_i^h, q_i^h; \mathbf{u}^h, p^h\right) - \left(v_i'^h, v_{\mathrm{T}}' \left(\nabla \mathbf{u}^h\right) \cdot \mathbf{n}\right)_{\Gamma_i'} = \left(v_i^h, f\right)_\Omega,$$

(27)

since it is guaranteed by the definition of S^{pm} that $\left(\nabla \bar{\mathbf{u}}^h\right) \cdot \mathbf{n} = 0$ and, hence, $\left(\nabla \mathbf{u}^h\right) \cdot \mathbf{n} = \left(\nabla \mathbf{u}'^h\right) \cdot \mathbf{n}$ on Γ_i' The validity of (27) for S^{pm} in the FVM provides substantial computational savings. All calls of the scale-separating computational subroutine during the actual solution procedure, for example, at the beginning of each solver iteration step for determining the updated large-scale velocity field for the residual calculation, are not required for S^{pm}, in contrast to S^{sm}. Note that, both in (25) and (27), the subgrid viscosity term directly acts only on the *small* resolved scales, in contrast to (14). The indirect influence on the large resolved scales, however, is ensured due to the inherent coupling of the large and small resolved scales.

4 Subgrid-scale modeling

Two different versions of the Smagorinsky model [37] are used for the calculation of the subgrid viscosity v_{T} and v_{T}', respectively. The subgrid viscosity v_{T} is given as

$$v_{\mathrm{T}} = (C_{\mathrm{S}} h)^2 |\varepsilon, \mathbf{u}^h|,$$

(28)

where ε denotes the rate-of-velocity tensor depending on the complete resolved velocity $\mathbf{u}^h$, which is defined as the symmetric part of the spatial gradient of the velocity subject to

$$\varepsilon\left(\mathbf{u}^h\right) = \frac{1}{2}\left[\nabla \mathbf{u}^h + \left(\nabla \mathbf{u}^h\right)^T\right],$$

(29)

and C_{S} the Smagorinsky model constant. In the case of v_{T}', the dependence is restricted to the small-scale part of the velocity as

$$v_{\mathrm{T}}' = (C_{\mathrm{S}} h)^2 |\varepsilon\left(\mathbf{u}'^h\right)| = (C_{\mathrm{S}} h)^2 |\varepsilon\left(\mathbf{u}^h - \bar{\mathbf{u}}^h\right)|.$$

(30)

The actual evaluation of (28) or (30), respectively, is performed in every child control volume Ω_i, so that a value

$v_{T,i}$ or $v_{T,i}'$, respectively, in every child control volume is obtained. The characteristic length scale of the child control volume Ω_i is assumed to be the cube root of the respective measure, i.e.,

$$h_i = |\Omega_i|^{\frac{1}{3}}.$$

(31)

The choice of the constant C_{S} in the case of turbulent flow in a diffuser is not an easy one, since there appears to be an entire lack of available data for this case, to the best of the author's knowledge. For the channel flow simulations in [10], the constant was chosen to be 0.1, according to the original choice in [6], although this original choice was by no means designed for a multiscale LES in the present sense. This choice is maintained for the inflow channel simulations below. For the actual diffuser, a value of $C_{\mathrm{S}} = 0.18$ is applied. It represents the value obtained in Lilly's analysis (see, e.g., [30]), balancing turbulent kinetic energy production and dissipation (cf. [18]), but it has mainly been applied for homogeneous isotropic turbulence. However, this choice is supported by a simple comparison of values observed during dynamic calculations in the inflow channel and in the diffuser. Considering a volume-averaged value of C_{S} over the respective domain, values of approximately 0.15 and 0.25 are obtained in the inflow channel and in the diffuser, respectively (i.e., a ratio of about 0.6). Setting 0.1 in this ratio, a constant $C_{\mathrm{S}} \approx 0.17$ can be calculated for the diffuser based on this rough approximation, which is close to the chosen value 0.18.

In order to actually calculate C_{S} as a model *parameter*, the dynamic modeling procedure proposed in [9], which enables a computation of C_{S} as a function of time and position, is applied. The procedure was adapted in [10] to the particular scale separation used in the present work, and it is referred to [10] for elaboration. In order to account for potential numerical problems related to negative values of C_{S}, a special clipping proposed in [31] is performed.

5 Numerical simulations

5.1 Numerical setup

The diffuser geometry, which basically matches the experimental configuration in [2] and [36] as well as the numerical setup in [26] and [40], is shown in Fig. 1. The inlet plane is

located at $x_1 = -5$, followed by an inlet channel of length $5\delta_c$, where the inlet channel half-width δ_c, which matches the half-width of the preceding inflow channel, is set to be of unit length. The asymmetric diffuser of length $42\delta_c$ opens with an angle of $10°$. This corresponds to an expansion ratio of $h_{in}/h_{out} = 4.7$. It is followed by an outlet channel of height $9.4\delta_c$ and length of approximately $58\delta_c$, which locates the outlet plane at about $x_1 = 100$. The outlet channel length matches the one in [40] and is considerably longer than the one in [26]. Due to the relatively long distance between the last point of measurement and the outlet plane, any significant upstream influence of the outlet plane is minimized. Nevertheless, the recovery into a canonical channel flow will not be reached even within this longer outlet channel, see [2] and [26]. Both the upstream corner at $x_1 = 0$ and the downstream corner at $x_1 = 42$ are rounded with a radius of $r = 19.4$, where the curvature centers are located as shown in Fig. 1. The length of the domain in x_3-direction (i.e., orthogonal to the depiction in Fig. 1 is chosen to be $8\delta_c$, matching the spanwise length in [40] and representing the largest value for the spanwise length investigated in [26]. The inflow channel, in which the inflow velocity $\mathbf{u}^{in}$ is generated, matches the inlet channel in its dimensions in x_2- and x_3-direction. According to [40], an inflow channel length of $12\delta_c$ is chosen.

Flow at Reynolds number $Re_\tau = u_\tau \delta_c/\nu = 500$ is simulated in the inflow channel. The turbulent wall-shear velocity $u_\tau = \sqrt{\tau_w}$, where τ_w denotes the wall shear stress, and the channel half-width δ_c define the Reynolds number Re_τ besides the kinematic viscosity ν. The velocity at the outlet plane of the inflow channel represents the inflow velocity $\mathbf{u}^{in}$ for the diffuser. The Reynolds number for the flow in the diffuser is determined based on the streamwise bulk mean velocity u_b (i.e., $Re_b = u_b \delta_c/\nu$). In contrast to [40], where $\mathbf{u}^{in}$ was rescaled to match it with the inflow in [2] as closely as possible, no rescaling is performed in the present case. The intention of the present work is to achieve unmodified results for all tested methods as far as possible. The inflow channel and the diffuser itself are hereby considered as an integrated system. The respective values for u_b resulting from the inflow channel simulations will be given below. As will be seen, the corresponding Reynolds numbers Re_b range from about 10,200 to 11,200 and are, thus, higher than 9,000, which is the approximate Reynolds number in the aforementioned experimental and numerical studies. However, the flow appears to be insensitive to the Reynolds number in this higher Reynolds number range according to [26]. After the inflow channel flow simulations have been conducted, and the respective values for the streamwise bulk mean velocity u_b have been determined, all flow simulation results from the diffuser are scaled by those values (i.e., the velocity results are scaled by u_b and the wall static pressure and skin friction coefficients are scaled by u_b^2).

The inflow channel is spatially discretized using 80, 64, and 80 control volumes in x_1-, x_2-, and x_3-direction, respectively. The distribution of control volumes in the wall-normal direction obeys a cosine function, refining towards the walls for the parent grid, which contains 40, 32, and 40

control volumes in x_1-, x_2-, and x_3-direction, respectively (i.e., coarser by a factor of two in each direction with respect to the child grid). The isotropic hierarchical subdivision procedure is subsequently applied to obtain the child grid. The control volume lengths in the respective coordinate directions are $h_1 = 0.15$, $h_{2,min} = 0.0024$, $h_{2,min} = 0.049$, and $h_3 = 0.1$, which corresponds to $h_1^+ = 75$, $h_{2,min}^+ = 1.2$, $h_{2,max}^+ = 24.5$, and $h_3^+ = 50$ in non-dimensional length units $h^+ = hu_\tau/\nu$ Compared to the discretization of the inflow channel in [40], which employed 128 control volumes in each coordinate direction, less than 20% the number of control volumes are used in the present case.

The actual diffuser, including inlet and outlet channel, is discretized using 290, 64, and 80 control volumes in x_1-, x_2-, and x_3-direction, respectively. The respective parent grid contains 145, 32, and 40 control volumes in x_1-, x_2-, and x_3-direction, respectively. The control volumes are uniformly distributed in the spanwise direction as in the inflow channel. In the wall-normal direction, the same cosine function for refinement towards the walls for the parent grid is used as in the inflow channel, with the same isotropic hierarchical subdivision procedure subsequently applied. This leads to an equivalent distribution in the inlet channel, which is then spread in the asymmetric section of the diffuser. In the outlet channel, control volume lengths range from $h_{2,min} = 0.023$ to $h_{2,max} = 0.046$ in the wall-normal direction. In the streamwise direction, the following control volume distribution is employed: in the inlet channel, h_1 decreases linearly from 0.15 to 0.05, in the asymmetric diffuser section, h_1 increases linearly from 0.05 to 0.475, in the first section of the outlet channel (ranging from $x_1 = 42$ to $x_1 = 74.5$), h_1 increases linearly from 0.475 to 0.825, and in the remaining section of the outlet channel, the control volumes are uniformly distributed with $h_1 = 0.825$. Comparing the discretization of the diffuser to the finer discretization in [40], which employed 590, 100, and 110 control volumes in x_1-, x_2-, and x_3-direction, it is stated that less than 23% the number of control volumes are used in the present case.

Both for the inflow channel and the diffuser simulation, the time step δt is fixed to be 0.002. For the inflow channel simulation, this corresponds to a non-dimensional time step in wall units $\delta t^+ = \delta t u_\tau^2/\nu = 1.0$. 5,000 time steps are performed to allow the flow to develop, and the statistics as well as the inflow velocity data are collected during another 10,000 time steps. As a consequence, inflow data for 20 time units are available, which represents a sufficient period for a fluid particle to be convected over a distance roughly equal to the streamwise diffuser dimension including inlet and outlet channel. This corresponds to an overall averaging period of 10,000 in non-dimensional wall units $T^+ = T u_\tau^2/\nu$ for the statistics of the inflow channel simulation. In the actual diffuser simulation, 40,000 time steps corresponding to 80 time units are performed to allow the flow to develop, and the statistics are collected during another 40,000 time steps. Thus, the inflow data are recycled 8 times during the diffuser simulation. Using an inertial time scale $\tau(x_1) = 0.5 h_{diff}(x_1)/u_b(x_1)$ based on the local diffuser

height $h_{\text{diff}}(x_1)$ for scaling purposes, statistics are sampled over a period of more than $1{,}600\,\tau_{\text{in}}$ where τ_{in}, denotes the inertial time scale in the inlet channel. This averaging period is even longer than the one in [26] for their finest case ($1{,}280\,\tau_{\text{in}}$), which those authors claimed to be long enough to ensure converged statistics in the rear part of the diffuser. In [40], a longer averaging period of 100 time units after an also longer evolution period of 120 time units was chosen, using a smaller time step $\delta t = 0.0013$. Due to a matching choice for the time step as well as the discretization at the outlet plane of the inflow channel and the inlet plane of the diffuser, neither a temporal nor a spatial interpolation is necessary for the inflow velocity $\mathbf{u}^{\text{in}}$, in contrast to [40].

All numerical simulations in the upcoming section are conducted using the CDP-α code, which is an unstructured finite-volume-based CFD code designed for LES of variable density low Mach-number flows on very large grids using massively parallel computers. The main features are the use of a fractional-step procedure with a four-step scheme and a momentum interpolation method for unstructured colocated grids according to [27]. The Crank–Nicolson scheme, a fully implicit time-stepping scheme of second-order accuracy, is applied to the convective and viscous terms, and, furthermore, the non-linear convective term is linearized about the result from the previous time step. All spatial and temporal approximations are of second-order accuracy. Furthermore, discrete conservation of energy is enforced. The discrete representation of the convective and the pressure term are the crucial aspects for guaranteeing discrete conservation of energy in the numerical method underlying CDP-α. These issues are addressed in detail in [32]. The particular reconstruction for the pressure term used in the current version of CDP-α is described in [14]. Plots quantifying the discrete conservation of energy for a number of test problems may be found in [14] and [32]. The momentum equation in the first step of the fractional-step procedure is solved using a simple iterative SOR solution procedure. For the solution of the pressure Poisson equation in the third step of the fractional-step procedure, an algebraic multigrid solver is used. It is referred to [15] for the details as well as some investigations concerning the performance of this multigrid solver. For the grid generation, the simple preprocessing program CART2CDP, which was already used for the grid generation inside the channel in [10], is modified, in order to generate grids inside the diffuser geometry according to Fig. 1.

5.2 Compared values and methods

In the inflow channel, the mean streamwise resolved velocity $\langle u_1^h \rangle$ is evaluated as well as the turbulent kinetic energy of the resolved scales, which reads

$$k^h = \frac{1}{2}\left(\langle u_1^h u_1^h + u_2^h u_2^h + u_3^h u_3^h \rangle \right.$$
$$\left. - \langle u_1^h \rangle \langle u_1^h \rangle - \langle u_2^h \rangle \langle u_2^h \rangle - \langle u_3^h \rangle \langle u_3^h \rangle \right). \quad (32)$$

Mean values in the inflow channel are obtained by averaging over all time steps of the statistical period as well as over the homogeneous x_1–x_3-planes. Both mean values are scaled by the wall-shear velocity u_τ or u_τ^2 respectively. The results from the inflow channel are compared to the DNS data for the case $Re_\tau = 590$ from the study in [33] in the respective diagrams. This does not exactly match the Reynolds number for the flow in the inflow channel, but it provides a rough indication where the results for a DNS at the actual Reynolds number $Re_\tau = 500$ should be expected.

In the diffuser, the mean streamwise resolved velocity $\langle u_1^h \rangle$ is evaluated as profiles in the wall-normal direction at four different locations in streamwise direction. These locations are distributed along the diffuser as follows: one behind the entry to the asymmetric diffuser section ($x_1 = 6.4$), one in the middle ($x_1 = 22.4$), one close to the end ($x_1 = 38.4$), and one in the outlet channel ($x_1 = 58.4$). These locations correspond to locations where experimental as well as numerical results are available from the studies in [36] and [40]. At the same locations, the root-mean-square values for the streamwise and wall-normal resolved velocities $u_1^{h,\text{rms}}$ and $u_2^{h,\text{rms}}$ are evaluated. All mean and root-mean-square values in the diffuser are obtained by averaging over all time steps of the statistical period as well as over the homogeneous x_3-direction. Both mean and root-mean-square velocities are scaled by the streamwise bulk mean velocity u_{b}. The results for the mean and root-mean-square values of the velocity are compared to the numerical results from [40], hereafter referred to as "Wu-LES", and to the experimental results from [36], hereafter referred to as "Obi-experiment".

Both along the upper and lower wall of the diffuser, the wall static pressure coefficient defined as

$$C_{p\text{w}}(x_1) = \frac{\langle p_\text{w}^h \rangle(x_1) - \langle p_\text{w}^h \rangle(x_1 = -5)}{\frac{1}{2}\rho u_\text{b}^2}, \quad (33)$$

where p_w^h denotes the discrete pressure value at the wall, and the skin friction coefficient subject to

$$C_{\text{f}}(x_1) = \frac{\langle \tau_\text{w}^h \rangle(x_1)}{\frac{1}{2}\rho u_\text{b}^2}, \quad (34)$$

where τ_w^h denotes the discrete value of the wall shear stress, are evaluated as functions of the streamwise direction x_1 respectively. In both (33) and (34), the fluid density ρ is assumed to be of unit value. The results for the two coefficients in (33) and (34) are compared to the numerical data from the Wu-LES. Furthermore, the results for the skin friction coefficient are compared to the experimental data from [2], hereafter referred to as "Buice-experiment". Due to the fact that the reference pressure value was chosen at a different location in the Buice-experiment, namely $x_1 = -3.4$ for the present configuration, it is not possible to accurately compare the results for the wall static pressure coefficient as well.

Finally, the mean value of the dynamically determined model parameter $\langle C_{\text{S}} \rangle$ as well as the mean value of the ratio of the subgrid viscosity ν_{T} or ν_{T}', respectively, to the physical viscosity ν are evaluated at the four locations specified above.
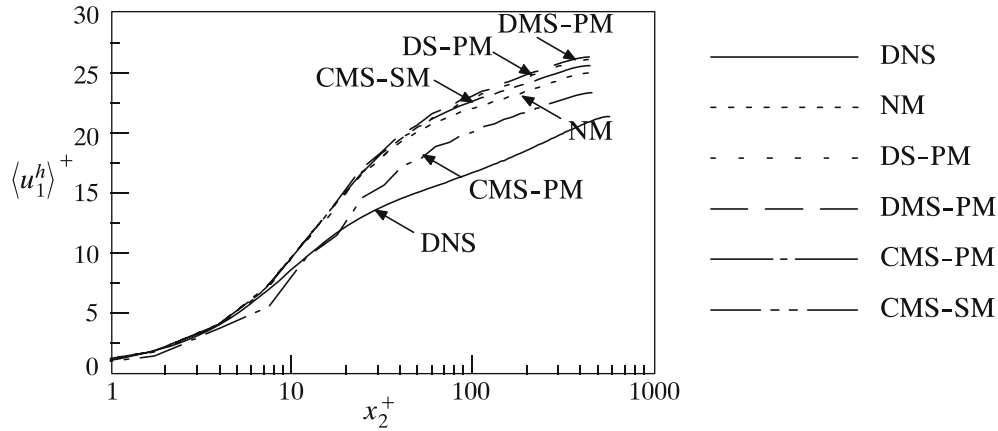
Fig. 3 Mean streamwise velocity in the inflow channel

This provides insight into the amount of subgrid viscosity introduced by the various methods.

As in [10], three different methods are investigated:

- the dynamic Smagorinsky (DS) model in a non-multiscale application subject to (14), with the subgrid viscosity subject to (28),
- the constant-coefficient-based Smagorinsky model within the multiscale environment (CMS) subject to (25) or (27), respectively, with the subgrid viscosity subject to (30), and
- the dynamic Smagorinsky model within the multiscale environment (DMS) subject to (25) or (27), respectively, with the subgrid viscosity subject to (30).

All of these methods are analyzed for the scale-separating operator S^{pm} In the following diagrams, the abbreviation DMS-PM, for instance, indicates the variational multiscale LES incorporating a dynamic Smagorinsky model, with the scale-separating operator S^{pm} applied. The scale-separating operator S^{sm} is only investigated for CMS, since this method revealed the most notable differences between the scale-separating operators for the test case in [10]. Results are also reported for simulations using no model at all (NM), which represents a coarse (i.e., not sufficiently resolved) DNS. Based on evaluations in [10], the characteristic length scale ratio for the DS- and DMS-simulations using S^{pm} is set to 2.5. The Wu-LES, which the results are compared to, applied the same dynamic Smagorinsky model in a traditional non-multiscale LES (i.e., DS), including the same special clipping according to [31]. However, the differences to the DS method used in the present study refer to, on the one hand, the fact that the Wu-LES used traditional discrete smooth filters instead of the multigrid scale-separating operators for the dynamic modeling and, on the other hand, to the discretization, both in terms of the number of control volumes and in the generation of the grid, as outlined above.

Evaluating the necessary computational effort provides the following numbers. Setting the computational effort for NM to 1.0, the relative measures for CMS-PM, CMS-SM, DS-PM, and DMS-PM are approximately 1.08, 1.34, 1.27,

and 1.32, respectively. These numbers are even more impressively in favor of CMS-PM than the ones for the channel in [10]. Thus, it is confirmed that CMS in combination with PM is a very efficient method computationally, in the present case substantially more efficient than, for instance, DS. Using the scale-separating operator SM, the numbers increase drastically for CMS. Less effort is required for PM compared to SM, because of the opportunity to use (27) in preference to (25), which obviates the execution of a potential scale-separating operation at the beginning of each iteration within the SOR solver, as already mentioned in Sect. 3.

5.3 Results from the inflow channel

Figures 3 and 4 depict the mean streamwise velocity and the turbulent kinetic energy, respectively, for the inflow channel. As already observed in [10], the large numerical error introduced by a second-order accurate method in combination with a relatively coarse discretization (see also, e.g., [29, 38]) affects CMS-PM to a far lesser extent than the other methods towards the channel center. It is considerably closer to the DNS profile in this section of the channel than NM, CMS-SM, DS-PM, and DMS-PM. Despite the higher accuracy in the inertial layer (usually expected to start at $x_2^+ = 30$), CMS-PM underpredicts the velocity profile in the buffer layer (usually expected to range from $x_2^+ = 5$ to $x_2^+ = 30$). The profile for the turbulent kinetic energy using CMS-PM shows a much better agreement for the height of the peak in comparison to the DNS profile than all other methods. This observation also corresponds to the one in [10]. A remarkable difference to the results in [10] is also noted. Here, DS-PM performs slightly better than DMS-PM, both in terms of the mean streamwise velocity and the turbulent kinetic energy. This may probably be attributed to the slightly coarser discretization in x_1- and x_3-direction. Coarsening the discretization seems to affect the results obtained with a dynamic model in a multiscale formulation more severely than the ones obtained with a dynamic model in a non-multiscale formulation. Similar observations in the context of homogeneous
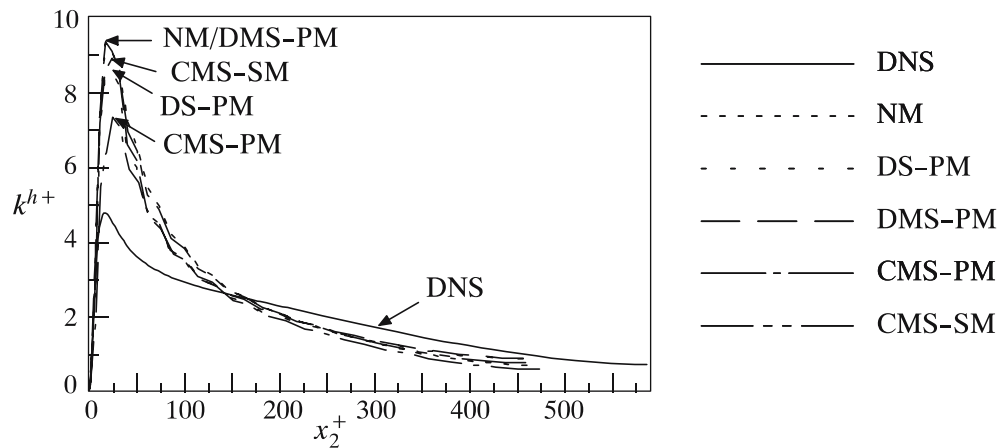
Fig. 4 Turbulent kinetic energy in the inflow channel
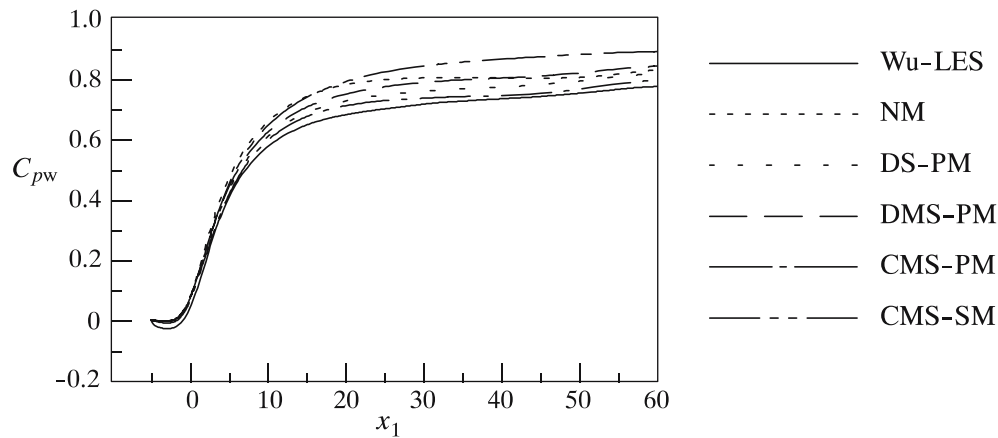
Fig. 5 Wall static pressure coefficient along the upper wall of the diffuser

Table 1 Streamwise bulk mean velocity u_b and corresponding Reynolds number Re_b

	Streamwise bulk mean velocity	Corresponding Reynolds number
Wu-LES	18.19	9,095
NM	21.56	10,778
DS-PM	22.20	11,100
DMS-PM	22.32	11,160
CMS-PM	20.39	10,195
CMS-SM	21.93	10,965

isotropic turbulence were made in [21]. Nevertheless, both dynamic methods are clearly outperformed by the constant-coefficient-based CMS, but only in combination with the projective scale-separating operator.

Table 1 contains the values for the streamwise bulk mean velocity u_b and the corresponding Reynolds numbers Re_b as a result of the inflow channel simulations. The computed values for the finer discretization of the Wu-LES are also given for comparison. The values for CMS-PM are the closest compared to the ones from the Wu-LES. All following results obtained in the diffuser are scaled by the streamwise bulk mean velocity or its squared value, respectively.

5.4 Results for wall static pressure and skin friction coefficients

The results for the wall static pressure coefficient along the upper and lower wall of the diffuser are displayed in Figs. 5 and 6, respectively. Overall, it is stated that all methods tend to overpredict C_{pw} compared to the results from the Wu-LES, and that the results are qualitatively the same for both the upper and the lower wall. The most remarkable observation is that the best and worst approximations are both produced by the same method. CMS-PM yields results which are very close to the results from the Wu-LES. On the contrary, CMS-SM yields by far the worst results. The second best results are obtained with DS-PM, which slightly outperforms DMS-PM. NM produces the worst results in terms of the pressure *gradient* component in streamwise direction. It predicts the highest value of all methods for the adverse pressure gradient at the diffuser throat and further downstream, and then changes relatively rapidly again, almost predicting a slightly favorable pressure gradient in the rear part of the diffuser, where a slightly adverse pressure gradient is expected.
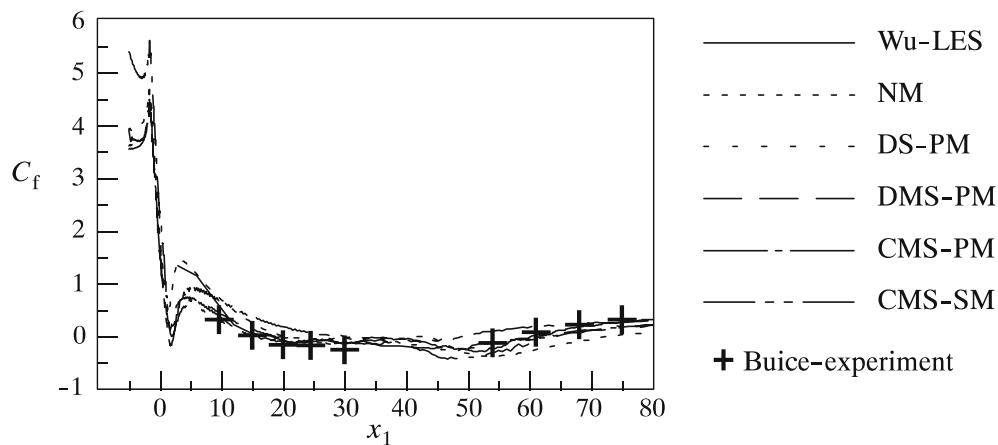
Figures 7 and 8 depict the results for the skin friction coefficient along the upper and lower wall of the diffuser,
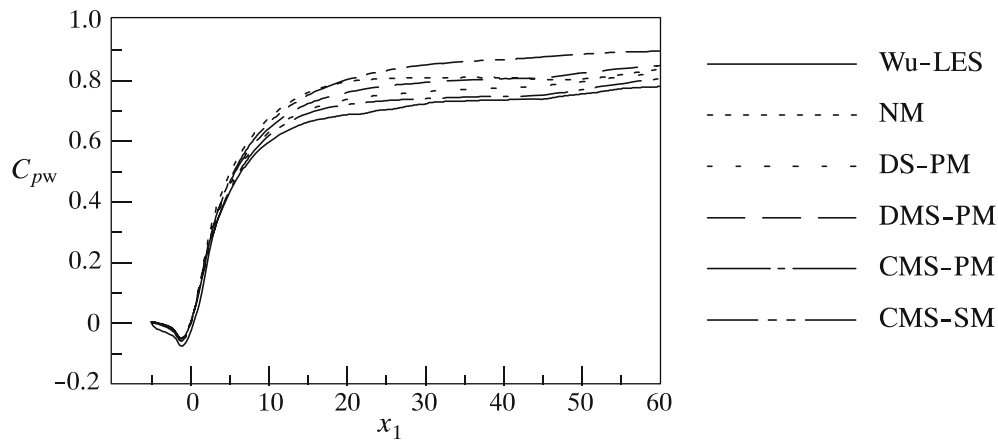
Fig. 6 Wall static pressure coefficient along the lower wall of the diffuser
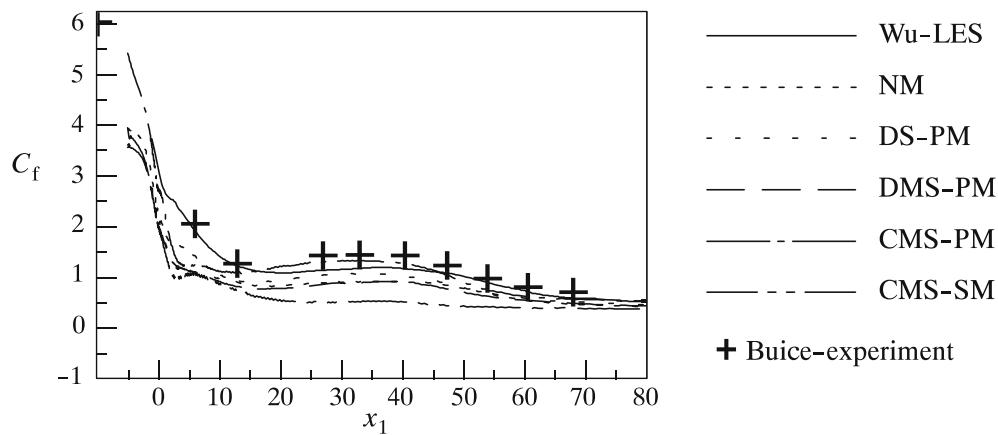
Fig. 7 Skin friction coefficient (factor 1,000) along the upper wall of the diffuser

Fig. 8 Skin friction coefficient (factor 1,000) along the lower wall of the diffuser

respectively. Results from the Wu-LES are not available for the inlet channel at both walls. At the lower wall, the first value was measured at $x_1 \approx 10$ in the Buice-experiment. Nevertheless, the values for the inlet channel are also included for the present methods in both diagrams. Qualitative comparison with the respective results in [26] confirm the

reasonability of the results in the inlet channel, in particular the abrupt drop of C_f to approximately zero close to the diffuser throat at the lower deflected wall.

For the upper wall, it is stated that all methods tend to underpredict C_f compared to the results from the Wu-LES and the Buice-experiment, with one exception. The worst re-
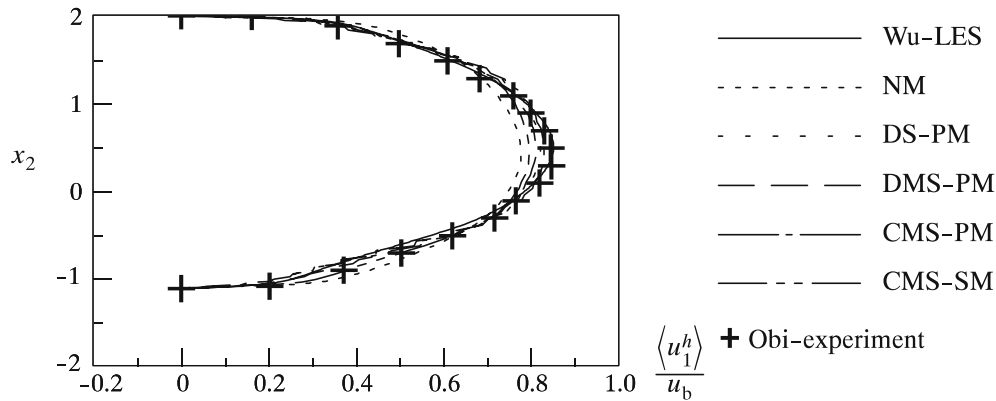
Fig. 9 Mean streamwise velocity at $x_1 = 6.4$
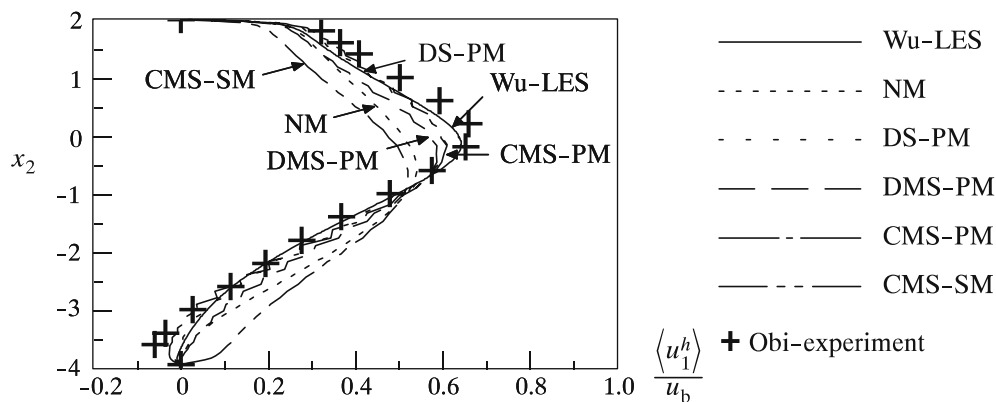
Fig. 10 Mean streamwise velocity at $x_1 = 22.4$

sults are again produced by CMS-SM. The profile for NM is closest to the ones from the Wu-LES and the Buice-experiment immediately behind the diffuser throat, but gets worse in its prediction further downstream. DS-PM yields a fairly good prediction throughout the diffuser, and DMS-PM again produces worse results than DS-PM. Although the results for CMS-PM are worse than the ones for NM immediately behind the diffuser throat, the predicition is again the best overall. It is the only method yielding results which almost match the experimental results in the section of the diffuser between $x_1 \approx 18$ and $x_1 \approx 46$ at the upper wall. In this part of the diffuser, which is approximately the region where the flow is separated, as will be seen below, CMS-PM appears to produce even better results than the substantially finer discretized Wu-LES. Furthermore, it seems to be the only one of the present methods which would have been able to predict the first point from the Buice-experiment at $x_1 \approx -10$, if the inlet channel had been elongated. A complete comparison at the lower wall may only be done from $x_1 \approx 10$, where the experimental data is available. After producing results close to the one from the Wu-LES immediately behind the diffuser throat, NM gets worse in its prediction further downstream. CMS-SM overpredicts the profile from $x_1 \approx 10$ throughout the diffuser. DS-PM, DMS-PM, and CMS-PM yield very similar results at the lower wall, representing a very good

prediction from $x_1 \approx 15$ throughout the diffuser compared to both the data from the Wu-LES and the Buice-experiment.

5.5 Results for mean velocity and root-mean-square velocities

In Figs. 9, 10, 11, and 12, the profiles for the mean streamwise velocity at the four locations along the diffuser specified above are displayed. Behind the entry to the asymmetric diffuser section, all methods predict a velocity profile which is in qualitative agreement with the ones from the Wu-LES and the Obi-experiment, although all of them underpredict the maximum velocity, see Fig. 9. The best prediction is produced by CMS-PM followed by DS-PM, DMS-PM, CMS-SM, and NM in descending order of their quality of approximation. CMS-PM even appears to underpredict the experimental data by approximately the same amount as the Wu-LES overpredicts. The second location depicted in Fig. 10 is slightly more than halfway down the diffuser, and the flow separation, which should be expected at $x_1 \approx 16$ according to the Buice-experiment, has already taken place. By observing Fig. 10 as well as Figs. 11 and 12, it is apparent that CMS-SM is inadequate, since it is the only method failing to predict the flow separation. The best approximation of the results from
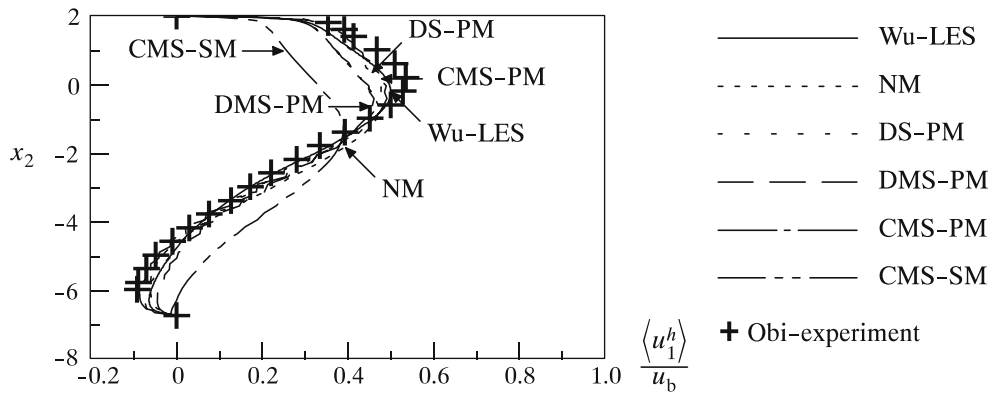
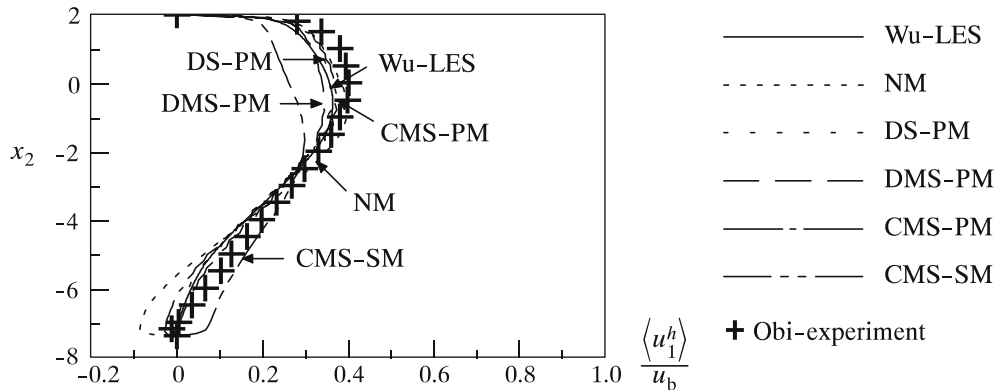**Fig. 11** Mean streamwise velocity at $x_1 = 38.4$

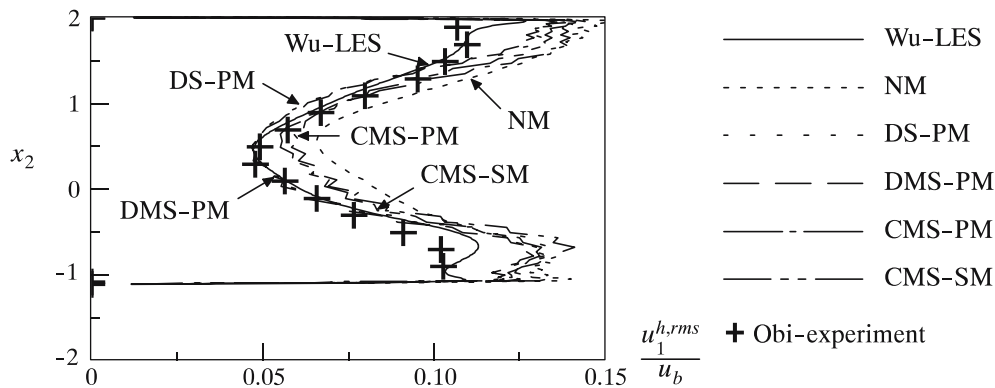**Fig. 12** Mean streamwise velocity at $x_1 = 58.4$

Fig. 13 Root-mean-square streamwise velocity at $x_1 = 6.4$

the Obi-experiment in Fig. 10 is provided by CMS-PM and the second best by DS-PM, both being even closer to the experimental data than the Wu-LES towards the lower wall. Compared to the experimental data, the Wu-LES does not predict the separation point as accurately as CMS-PM and DS-PM. At the next location further downstream depicted in Fig. 11, CMS-PM almost matches the experimental data in the lower part of the diffuser predicting the reversed flow very accurately. In the outlet channel, this very good approximation cannot be completely maintained, see Fig. 12. DMS-PM is less accurate at all three locations shown in Figs. 10,

11, and 12. Aside from CMS-SM, NM produces the worst prediction, with the exception of Fig. 11 (i.e., close to the end of the asymmetric diffuser section), where it is, at least, slightly better than DMS-PM. However, the most obvious failure of NM is its clear overestimation of the recirculating velocity in the outlet channel. Thus, it does not provide a reasonable approximation of the flow separation as well as the reattachment point, which should be expected at $x_1 \approx 52$ according to the Buice-experiment.

The profiles for the root-mean-square velocity in streamwise direction are shown in Figs. 13, 14, 15, and 16. Behind
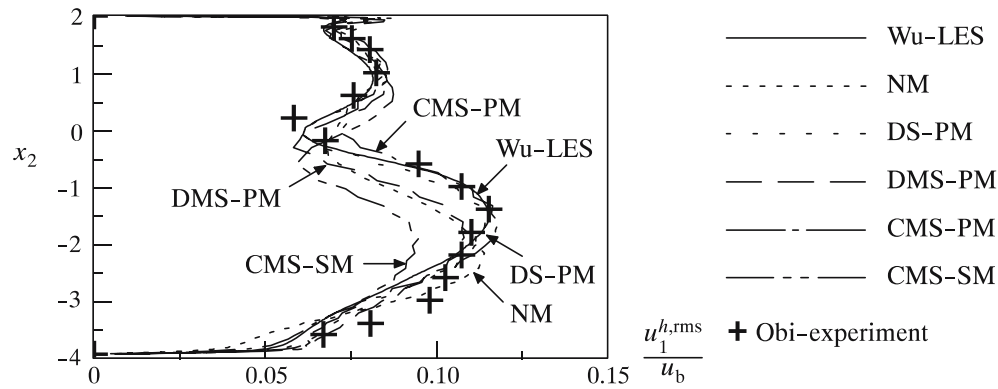
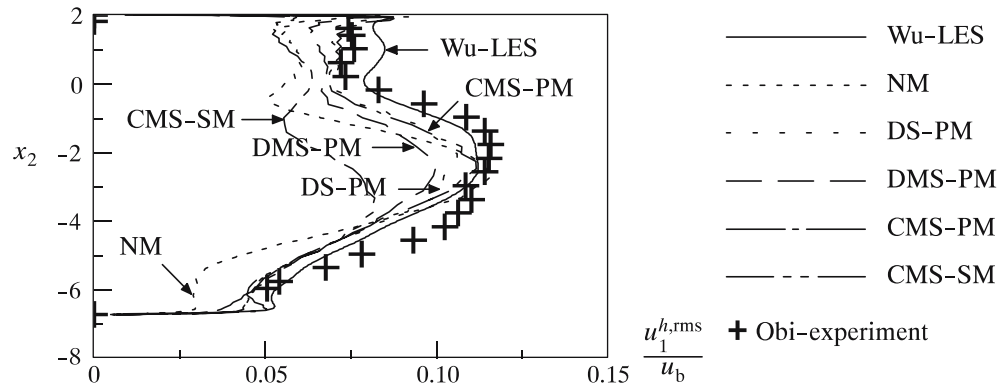**Fig. 14** Root-mean-square streamwise velocity at $x_1 = 22.4$

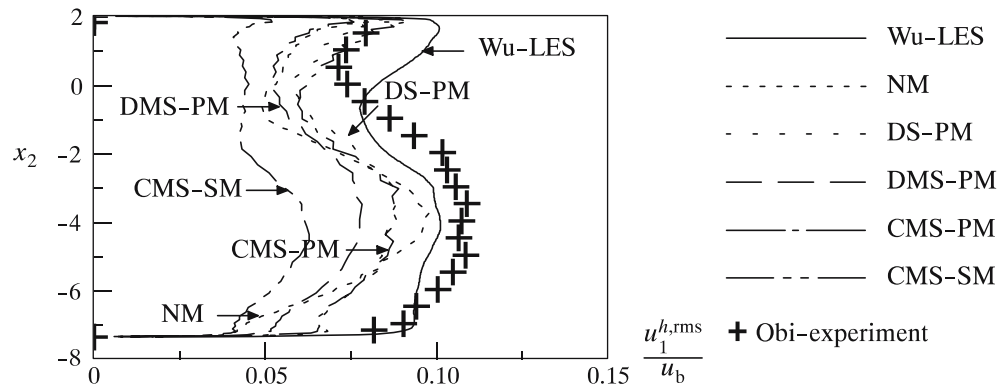**Fig. 15** Root-mean-square streamwise velocity at $x_1 = 38.4$

Fig. 16 Root-mean-square streamwise velocity at $x_1 = 58.4$

the entry to the asymmetric diffuser section, the best approximations are provided by DS-PM and DMS-PM, see Fig. 13. CMS-PM and CMS-SM depart further from the profiles from the Wu-LES and the Obi-experiment in this section of the diffuser, and NM is considerably far away from the reference profiles. As in the context of the mean streamwise velocity, the picture changes as soon as one proceeds further downstream. Figures 14, 15, and 16 indicate that the predictions for CMS-PM and DS-PM are of similar quality and give the best approximations. DMS-PM performs slightly worse, and CMS-SM provides a bad approximation overall. It should be noted that CMS-PM, DS-PM, and DMS-PM provide even

better results than the Wu-LES compared to the experimental data towards the upper wall of the diffuser further downstream in Figs. 15 and 16. NM produces mixed results with good approximations in the area around the centerline of the diffuser and very bad approximations towards the walls, in particular close to the end of the asymmetric diffuser section and in the outlet channel, see Figs. 15 and 16.

Figures 17, 18, 19, and 20 display the profiles for the root-mean-square velocity in wall-normal direction. In contrast to the situation for the streamwise root-mean-square velocity, the best approximations are provided by CMS-PM and CMS-SM at the entry to the asymmetric diffuser section,
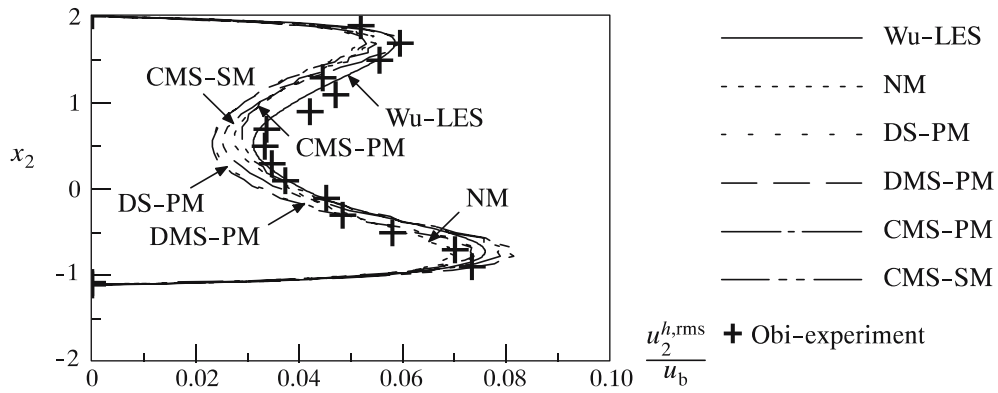
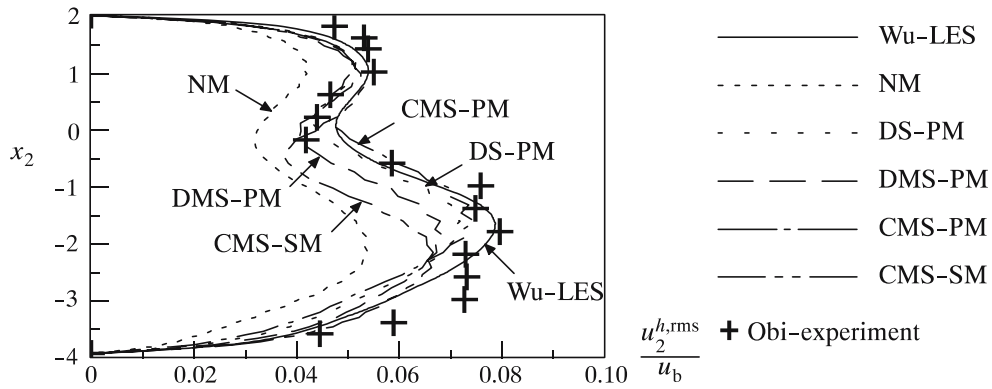**Fig. 17** Root-mean-square wall-normal velocity at $x_1 = 6.4$

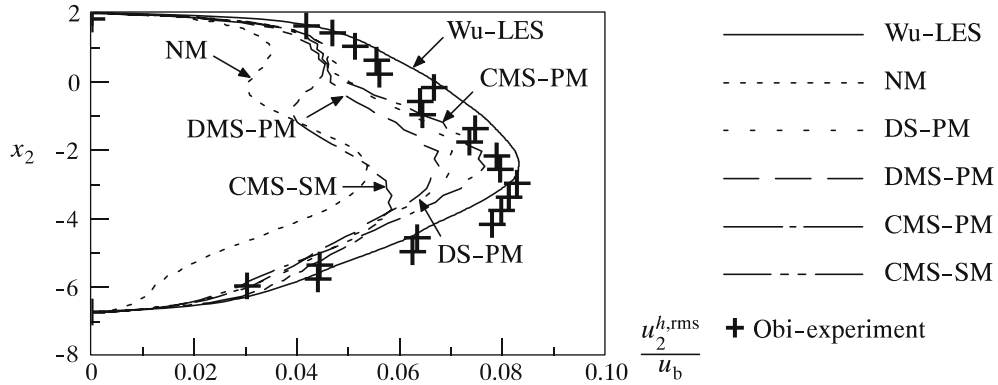**Fig. 18** Root-mean-square wall-normal velocity at $x_1 = 22.4$

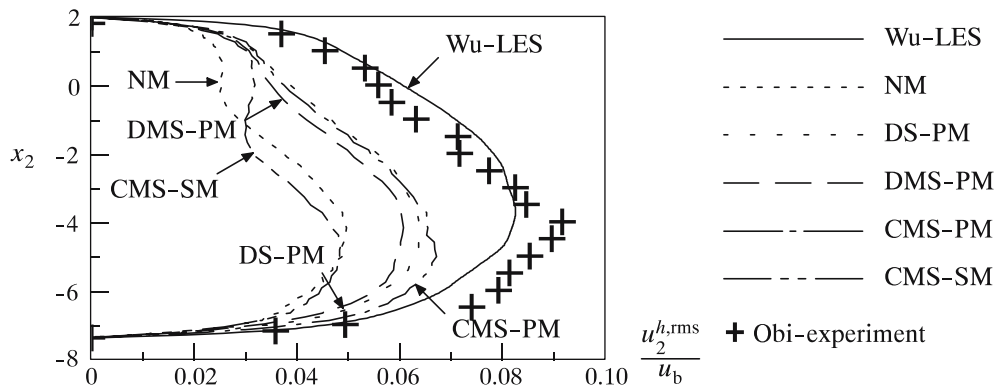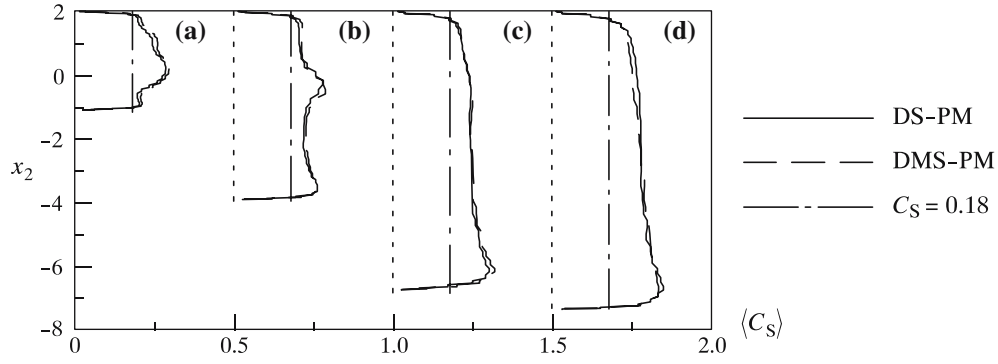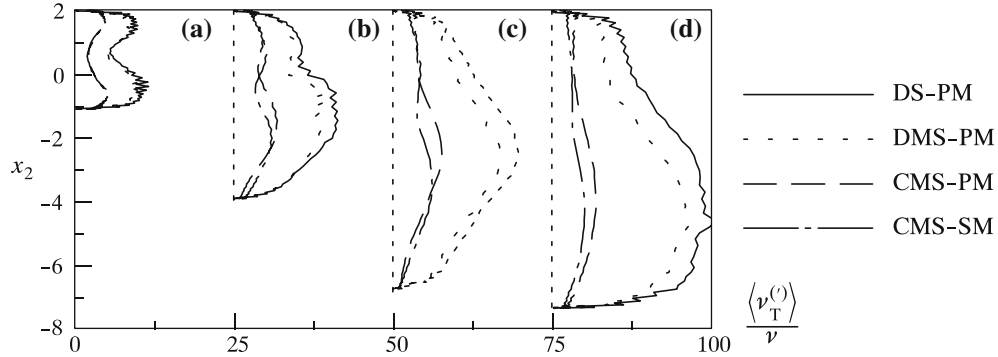**Fig. 19** Root-mean-square wall-normal velocity at $x_1 = 38.4$

Fig. 20 Root-mean-square wall-normal velocity at $x_1 = 58.4$

Fig. 21 Mean value of model parameter C_S: (**a**) $x_1 = 6.4$; (**b**) $x_1 = 22.4(+0.5)$; (**c**) $x_1 = 38.4(+1.0)$; (**d**) $x_1 = 58.4(+1.5)$

Fig. 22 Mean ratio of subgrid and molecular viscosity: (**a**) $x_1 = 6.4$; (**b**) $x_1 = 22.4(+25)$; (**c**) $x_1 = 38.4(+50)4$; (**d**) $x_1 = 58.4(+75)$

see Fig. 17. This time, DS–PM and DMS–PM are further away from the profiles from the Wu-LES and the Obi-experiment in this section of the diffuser. NM produces a fairly good prediction. Further downstream and in the outlet channel, CMS-SM and NM yield very poor approximations of the reference data, see Figs. 18, 19, and 20. The profiles for CMS-PM and DS-PM are again of similar quality and give the best predictions. DMS-PM performs slightly worse than DS-PM again.

5.6 Investigating the dynamically determined model parameter and the subgrid viscosity

Figure 21 displays the profiles for the mean value of the dynamically determined parameter of the Smagorinsky model $\langle C_S \rangle$ at the various locations along the diffuser. For comparison, the constant $C_S = 0.18$ used for CMS-PM and CMS-SM is also indicated. The curves for $\langle C_S \rangle$ cross the line for the constant already close to the walls in each case. This is in contrast to the results for the channel in [10], where the profiles for $\langle C_S \rangle$ using the scale-separating operator PM did not cross the constant line anywhere in the channel. The reason for this different picture is the use of a different clipping within the dynamic modeling procedure, which yields substantially higher values for the parameter.

In Fig. 22, the profiles for the mean value of the ratio of the subgrid viscosity ν_T or ν_T' respectively, to the molecular viscosity ν are evaluated at the various locations along

the diffuser. The situation in Fig. 22 is a consequence of the one in Fig. 21: a substantially higher amount of subgrid viscosity is introduced by the dynamic models throughout most of the diffuser. The only part of the diffuser where the constant-coefficient-based models add more subgrid viscosity is very close to the upper and lower wall, due to the fact that the constant model parameter does not approach zero towards the wall. This particular situation close to the walls is more clearly depicted in Fig. 23, where it is zoomed in on the upper wall of the diffuser. The profiles in Fig. 22 are qualitatively similar to the ones in [26], Fig. 14. Kaltenbach et al. [26], however, applied a different dynamic modeling procedure. They averaged the values for C_S over the homogeneous spanwise direction, and, presumably, although it is not mentioned in the publication, used the traditional clipping procedure, which simply sets negative values to zero. Furthermore, those authors used a discrete smooth filter based on the trapezoidal rule for the separation of scales within the dynamic modeling procedure, which has been shown to generally yield higher values for in C_S [10]. Figure 22d shows that the maximum value for the viscosity ratio at the location in the outlet channel is about 25. Behind the entry to the asymmetric diffuser section, a maximum ratio of about 12 is already reached, see Fig. 22a. Maximum values at comparable locations in [26] are 6 and 2.5, respectively, representing considerably smaller values. The already addressed issue of using a different dynamic modeling procedure with different scale separation should, together, not
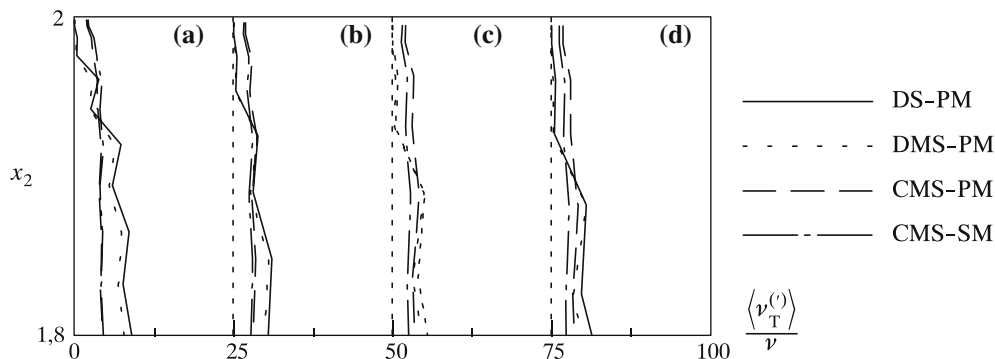
Fig. 23 Zoomed in on the upper wall of the diffuser with respect to the results depicted in Fig. 22

cause such an increase in the present case. Thus, the considerably coarser discretization may be identified as the actual reason for this absolute increase in the amount of subgrid viscosity.

Aside from an analysis of the absolute value of the subgrid viscosity, the more interesting question in the context of the present study concerns the relative amount of subgrid viscosity introduced by the various methods. In a specific investigation in [10], it has been found out that the essential reason for the good results obtained with CMS-PM can be traced back to the addition of a substantial amount of subgrid viscosity to the small resolved scales particularly in the buffer layer of the channel (i.e., relatively close to the walls). A very intense dissipation has to be expected in the buffer layer, according to, e.g., analyses of DNS databases in [16], underlining the necessity to let a considerably high amount of subgrid viscosity act particularly on the small scales in this region. It is referred to [10] for further discussion.

A reason for the relatively better performance of DS-PM and DMS-PM in comparison to CMS-PM in the present case might be attributed to the fact that, due to the generally higher values for C_S as a result of the present dynamic modeling procedure, a higher amount of subgrid viscosity is also added towards the walls. Note that the subgrid viscosity is added to *all* resolved scales for DS-PM. Nevertheless, there is a relatively small range close to the walls and outside of the viscous sublayer where the constant-coefficient-based Smagorinsky model still introduces a considerably higher amount of subgrid viscosity. This might still be one of the reasons for the better overall performance of CMS-PM compared to DS-PM and, in particular, DMS-PM.

6 Conclusions

Variational multiscale LES has been applied to turbulent flow in a diffuser. Turbulent flow in a diffuser represents a challenging test case, in particular due to the appearance of flow separation, which is caused by an adverse pressure gradient, and subsequent reattachment. Two different scale-separating operators based on multigrid operators, which are basically applicable within both a finite element and a finite volume method, have been used for separating large re-

solved scales and small resolved scales. Dynamic as well as constant-coefficient-based subgrid-scale modeling has been employed within the variational multiscale LES. The results have been compared to results obtained by using dynamic subgrid-scale modeling within the traditional non-multiscale LES. All approaches have been implemented in a second-order energy-conserving finite volume method particularly suited for applications on hybrid unstructured grids in complex geometries. The results obtained by the various approaches have been compared to results from a recent non-multiscale LES with dynamic subgrid-scale modeling performed on an approximately five times finer grid and experimental results.

The results have led to the following conclusions.

- The constant-coefficient-based variational multiscale LES using the projective scale-separating operator (CMS-PM) has produced the most accurate results for the wall static pressure coefficient and the skin friction coefficient along the diffuser as well as for the mean velocity in streamwise direction and the root-mean-square velocity in wall-normal direction. Within the flow separation region, CMS-PM has provided even better predictions of the skin friction coefficent and the mean streamwise velocity, respectively, than a traditional LES on a considerably finer grid compared to the experimental results.
- CMS-PM and the non-multiscale LES with dynamic subgrid-scale modeling (DS-PM) have yielded the most accurate results for the root-mean-square velocity in streamwise direction, both being of similar accuracy overall for these values.
- The constant-coefficient-based variational multiscale LES using the smoothing, non-projective scale-separating operator (CMS-SM) has failed to predict the flow separation and reattachment at the lower wall. As a result, this scale-separating operator should be disqualified from further use.
- The variational multiscale LES with dynamic subgrid-scale modeling using the projective scale-separating operator (DMS-PM) has produced worse predicitions compared to DS-PM for almost all investigated values.
- CMS-PM is by far the computationally most efficient approach of all approaches considered in the present study.

In particular, it reduces the computing time by about 18% compared to DS-PM. This is an even larger reduction compared to the channel flow simulations in [10], where the computing time was reduced by about 5%.

The results from a previous study in [10], where the same methods and scale-separating operators were tested for turbulent flow in a channel, have also been mirrored in the present study by reporting the results from the independently simulated inflow channel. Taking into account the results from both test cases, comprehensive conclusions may be formulated as follows:

- Taking into account all aspects investigated in the context of the channel and the diffuser, CMS-PM has provided the most accurate predictions overall. Only one shortcoming has to be noted: a slight underprediction of the mean streamwise velocity profile in the buffer layer of the channel.
- Aside from the observation that it produces the best results overall, CMS-PM also represents the most computationally efficient approach. This advantage of CMS-PM appears to increase with increasing problem size, as the comparison of the numbers for the present diffuser problem to the channel problem in [10] indicate.
- Both positive features linked with CMS-PM have to be attributed to the use of the projective scale-separating operator PM in this context. Already for the channel flow application in [10], PM has outperformed traditional discrete smooth filters, both in terms of quality of results and required computational effort. In the present work, the alternative scale-separating operator based on multigrid operators SM has failed to predict one of the most important aspects of the diffuser flow. Furthermore, a comparison of the computational effort emphasizes the superiority of PM over SM. With respect to the separation of scales, the essential feature of an orthogonal projective operator (i.e., self-adjoint projector), such as the one used in the present study, is that an explicit split into large and small scales is enabled, whereas for a non-projective operator "cross-scale" parts have to be expected (i.e., the large and the small scales are not explicitly separated). This has to be considered as the reason for the better results obtained via the projective scale-separating operator, see also [10] for further analysis of the operators.
- A surprising result is that DMS-PM has not proven to be a superior alternative to CMS-PM despite its more sophisticated (and, simultaneously, more expensive) subgrid-scale modeling approach. Throughout all investigations in [10] and in the present study, it has produced less accurate predictions. In contrast to the channel flow application, it has also yielded worse results than DS-PM in the diffuser application. The latter observation appears to be related to the relatively coarser discretization level applied to the diffuser, and, thus, is consistent with similar observations in [21] in the context of homogeneous isotropic turbulence.
- A potential explanation for the success of CMS-PM in the channel flow application has already been given in

[10] by analyzing the crucial benefit of adding a substantial amount of subgrid viscosity to the small resolved scales particularly in the buffer layer of the channel. Similar mechanisms might also guarantee its success in the present diffuser application.

Given the relative superiority of the results obtained using a constant-coefficient-based subgrid-scale model compared to a dynamic subgrid-scale model in the context of the variational multiscale LES, it appears to be worthwhile to further investigate variations of the model constant with respect to the "traditional" values in [6] and [30], which have been exclusively used in the present study. In the end, values for the model constant may perhaps be found which fit even better into the framework of the variational multiscale LES.

Finally, it has to be emphasized that all of these perceptions have been gained in the context of this particular implementation in a second-order accurate finite volume method. The use of different numerical methods, in particular spectral methods, can have a substantially different impact on crucial aspects of the flow, as Oberai et al. [35] were able to show for a simpler problem. However, a good performance of the approach under consideration in the present or similar computational environments (i.e., finite volume or finite element methods basically suited for unstructured grid applications) appears to be of particular relevance for future applications in more complex geometries.

References

1. Apsley DD, Lechziner MA (2000) Advanced turbulence modeling of separated flow in a diffuser. Flow Turbul Combust 63:81–112
2. Buice CU, Eaton JK (1997) Experimental investigation of flow through an asymmetric plane diffuser. TSD-107, Department of Mechanical Engineering, Stanford University
3. Calo VM (2004) Residual-based multiscale turbulence modeling: finite volume simulations of bypass transition. PhD Thesis, Department of Civil and Environmental Engineering, Stanford University, http: //www.ices.utexas. edu/∼victor/vmc-thesis.pdf
4. Collis SS (2001) Monitoring unresolved scales in multiscale turbulence modeling. Phys Fluids 13:1800–1806
5. Collis SS (2002) The DG/VMS method for unified turbulence simulation. AIAA Paper 2002–3124, St. Louis, MO, June 24–27
6. Deardorff JW (1970) A numerical study of three-dimensional turbulent channel flow at large Reynolds numbers. J Fluid Mech 41:453–465
7. Durbin P (1995) Separated flow computations with the $k - \varepsilon - v^2$ model. AIAA J 33:659–664
8. Farhat C, Rajasekharan A, Koobus B (2006) A dynamic variational multiscale method for large eddy simulations on unstructured meshes. Comput Methods Appl Mech Eng 195:1667–1691

9. Germano M, Piomelli U, Moin P, Cabot WH (1991) A dynamic subgrid-scale eddy viscosity model. Phys Fluids A 3:1760–1765
10. Gravemeier V (2006) Scale-separating operators for variational multiscale large eddy simulation of turbulent flows. J Comput Phys 212:400–435
11. Gravemeier V (2006) The variational multiscale method for laminar and turbulent flow. Arch Comput Methods Eng (in press)
12. Gravemeier V, Wall WA, Ramm E (2005) Large eddy simulation of turbulent incompressible flows by a three-level finite element method. Int J Numer Methods Fluids 48:1067–1099
13. Gullman-Strand J, Törnblom O, Lindgren B, Amberg G, Johansson AV (2004) Numerical and experimental study of separated flow in a plane asymmetric diffuser. Int J Heat Fluid Flow 25:451–460
14. Ham F, Iaccarino G (2004) Energy conservation in collocated discretization schemes on unstructured meshes. In: Annual research briefs – 2004, Center for Turbulence Research, Stanford University and NASA Ames Research Center, pp 3–14
15. Ham F, Apte S, Iaccarino G, Wu X, Herrmann M, Constantinescu G, Mahesh K, Moin P (2003) Unstructured LES of reacting multiphase flows in realistic gas turbine combustors. In: Annual research briefs – 2003, Center for Turbulence Research, Stanford University and NASA Ames Research Center, pp 139–160
16. Härtel C, Kleiser L, Unger F, Friedrich R (1994) Subgrid-scale energy transfer in the near-wall region of turbulent flows. Phys Fluids 6:3130–3143
17. Hellsten A, Rautaheimo P (eds) (1999) Proceedings of the 8th ERCOFTAC/IAHR/COST workshop on refined turbulence modeling. Helsinki University of Technology, Espoo, Finland, June 17, 18
18. Hughes TJR, Mazzei L, Jansen KE (2000) Large eddy simulation and the variational multiscale method. Comput Vis Sci 3:47–59
19. Hughes TJR, Mazzei L, Oberai AA, Wray AA (2001) The multiscale formulation of large eddy simulation: decay of homogeneous isotropic turbulence. Phys Fluids 13:505–512
20. Hughes TJR, Oberai AA, Mazzei L (2001) Large eddy simulation of turbulent channel flows by the variational multiscale method. Phys Fluids 13:1784–1799
21. Hughes TJR, Wells GN, Wray AA (2004) Energy transfers and spectral eddy viscosity in large eddy simulations of homogeneous isotropic turbulence: comparison of dynamic Smagorinsky and multiscale models over a range of discretizations. Phys Fluids 16:4044–4052
22. Iaccarino G (2001) Predictions of a turbulent separated flow using commercial CFD codes. J Fluids Eng 123:819–828
23. Jansen KE, Tejada-Martinez AE (2002) An evaluation of the variational multiscale model for large-eddy simulation while using a hierarchical basis. AIAA Paper 2002–0283, Reno, NV, January 14–17
24. Jeanmart H, Winckelmans GS (2002) Comparison of recent dynamic subgrid-scale models in turbulent channel flow. In: Proceedings of the summer program 2002, Center for Turbulence Research, Stanford University and NASA Ames Research Center, pp 105–116
25. John V, Kaya S (2005) A finite element variational multiscale method for the Navier–Stokes equations. SIAM J Sci Comp 26:1485–1503
26. Kaltenbach H-J, Fatica M, Mittal R, Lund TS, Moin P (1999) Study of flow in a planar asymmetric diffuser using large-eddy simulation. J Fluid Mech 390:151–185
27. Kim D, Choi H (2000) A second-order time-accurate finite volume method for unsteady incompressible flow on hybrid unstructured grids. J Comput Phys 162:411–428
28. Koobus B, Farhat C (2004) A variational multiscale method for the large eddy simulation of compressible turbulent flows on unstructured meshes – application to vortex shedding. Comput Methods Appl Mech Eng 193:1367–1383
29. Kravchenko AG, Moin P (1997) On the effect of numerical errors in large eddy simulations of turbulent flows. J Comput Phys 131:310–322
30. Lilly DK (1967) The representation of small-scale turbulence in numerical simulation experiments. In: Proceedings of the IBM scientific computing symposium on environmental sciences, Yorktown Heights, New York
31. Mahesh K, Constantinescu G, Apte S, Iaccarino G, Ham F, Moin P (2002) Progress toward large-eddy simulation of turbulent reacting and non-reacting flows in complex geometries. In: Annual research briefs – 2002, Center for Turbulence Research, Stanford University and NASA Ames Research Center, pp 115–142
32. Mahesh K, Constantinescu G, Moin P (2004) A numerical method for large-eddy simulation in complex geometries. J Comput Phys 197:215–240
33. Moser RD, Kim J, Mansour NN (1999) Direct numerical simulation of turbulent channel flow upto $Re_t = 590$. Phys Fluids 11:943–945
34. Oberai AA, Hughes TJR (2002) The variational multiscale formulation of LES: channel flow at $Re_t = 590$. AIAA Paper 2002–1056, Reno, NV
35. Oberai AA, Gravemeier V, Burton GC (2004) Transfer of energy in the variational multiscale formulation of LES. In: Proceedings of the summer program 2004, Center for Turbulence Research, Stanford University and NASA Ames Research Center, pp 123–132
36. Obi S, Aoki K, Masuda S (1993) Experimental and computational study of turbulent separating flow in an asymmetric plane diffuser. Ninth symposium on turbulent shear flows, Kyoto, Japan, August 16–19
37. Smagorinsky J (1963) General circulation experiments with the primitive equations. I. The basic experiment. Mon Weather Rev 91:99–164
38. Terracol M, Sagaut P, Basdevant C (2001) A multilevel algorithm for large-eddy simulation of turbulent compressible flows. J Comput Phys 167:439–474
39. Vreman AW (2003) The filtering analog of the variational multiscale method in large-eddy simulation. Phys Fluids 15:L61–L64
40. Wu X, Schlüter J, Moin P, Pitsch H, Iaccarino G, Ham F (2006) Computational study on the internal layer in a diffuser. J Fluid Mech 550:391–412